nature chemistry

ARTICLES

https://doi.org/10.1038/s41557-020-0493-5

Check for updates

Modulation of porosity in a solid material enabled by bulk photoisomerization of an overcrowded alkene

Fabio Castiglioni[1,3], Wojciech Danowski[2,3], Jacopo Perego[1], Franco King-Chi Leung[2], Piero Sozzani[1], Silvia Bracco[1], Sander J. Wezenberg[2]✉, Angiolina Comotti[1]✉ and Ben L. Feringa[2]✉

The incorporation of photoswitchable molecules into solid-state materials holds promise for the fabrication of responsive materials, the properties of which can be controlled on-demand. However, the possible applications of these materials are limited due to the restrictions imposed by the solid-state environment on the incorporated photoswitches, which render the photoisomerization inefficient. Here we present responsive porous switchable framework materials based on a bistable chiroptical overcrowded alkene incorporated in the backbone of a rigid aromatic framework. As a consequence of the high intrinsic porosity, the resulting framework readily responds to a light stimulus, as demonstrated by solid-state Raman and reflectance spectroscopies. Solid-state ^{13}C NMR spectroscopy highlights an efficient and quantitative bulk photoisomerization of the incorporated light-responsive overcrowded olefins in the solid material. Taking advantage of the quantitative photoisomerization, the porosity of the framework and the consequent gas adsorption can be reversibly modulated in response to light and heat.

Inspired by biological systems, a vast number of artificial molecular machines and switches, capable of elaborate structural dynamics, have been developed[1–4]. However, in solution, stimulated molecular motion is inevitably overwhelmed by isotropic thermal noise, which thereby precludes any form of collective action and the extraction of macroscopic work, as the molecules behave independently of one another[5–7]. On the contrary, solid-state organization can translate stimuli-controlled nanoscopic changes into useful material properties and preludes practical outputs. Thus, a challenging endeavour of current research is to organize molecular machines and switches in the solid state to impede random, thermal motion and amplify the mechanical effects along multiple length scales: this effort requires reliable strategies, which allow for restricting random motion and limit the degrees of freedom to selected modes, without impairment of the rotary or switching functions[8–10].

One strategy to achieve these goals is to use solid porous materials[11–15] which can incorporate switchable moieties and provide the free volume essential for unhindered dynamics, and thereby serve as a static scaffold for the flexible components. Indeed, it was demonstrated recently that molecular rotors[16–23], shuttles[24], switches[25] and motors[26] can display their designed motion when incorporated in porous architectures. The incorporation of photoresponsive molecular switches in solid materials, however, opens new opportunities to enrich the properties of these materials in a non-invasive manner with a high spatiotemporal precision[27,28]. This notion was illustrated in pioneering studies on photoresponsive porous solids functionalized with azobenzenes[29–39], dithienylethenes[40–48] or spiropyrans[49–51], which showed photomodulation of gas uptake, diffusion or guest release, respectively. However, bulk photoisomerization in solids suffers from a poor efficiency due to geometrical constraints and little light-penetration depth and is therefore limited to the near-surface region with the bulk of the material unaffected. So far, photoswitching in the bulk of solid materials has only been reported for rare cases of porous molecular crystals sustained by soft interactions[29] and dithienylethene-based metal–organic frameworks (MOFs)[42,45] which, because of their minimal structural arrangement, were shown to undergo efficient photoisomerization even in densely packed molecular crystals[48]. Hence, attaining bulk photoresponsivity, which involves a large structural motion that triggers substantial changes in properties, in robust solid materials remains a fundamental challenge.

Chiral overcrowded alkenes constitute a unique class of molecular photoswitches that exhibit a stereogenic centre in the vicinity of the olefinic bond. The steric congestion present in the system forces the molecule to adopt helical chirality, which is inverted in the photochemically generated metastable isomer (Fig. 1a)[52,53]. With the appropriate structural modification, the thermal stability of the metastable isomer can be increased by many orders of magnitude up to the point that unidirectional rotation is inhibited and the molecule can be operated as a chiroptical bistable switch[54]. It is known that the incorporation of overcrowded alkenes in soft-matter matrixes[55–60], or their anchoring to a surface[61], allows for the fabrication of materials that show unique, dynamic properties. Here we report the incorporation of an overcrowded alkene bistable chiroptical switch in highly porous and stable organic frameworks sustained by covalent bonds, herein referred to as porous switchable frameworks (PSFs), which allows for the switching of porosity and hence gas uptake. The overcrowded alkene was integrated into the framework backbone via its fluorenyl (stator) moiety to leave the naphthyl moiety (rotor) pendant (Fig. 1b). In the resulting architecture, the PSF backbone serves as a scaffold for the switchable unit without preventing the light-controlled large amplitude motion of

[1]Department of Materials Science, University of Milano Bicocca, Milan, Italy. [2]Centre for Systems Chemistry, Stratingh Institute for Chemistry, University of Groningen, Groningen, the Netherlands. [3]These authors contributed equally: Fabio Castiglioni, Wojciech Danowski. ✉e-mail: S.J.Wezenberg@lic.leidenuniv.nl; Angiolina.Comotti@unimib.it; B.L.Feringa@rug.nl

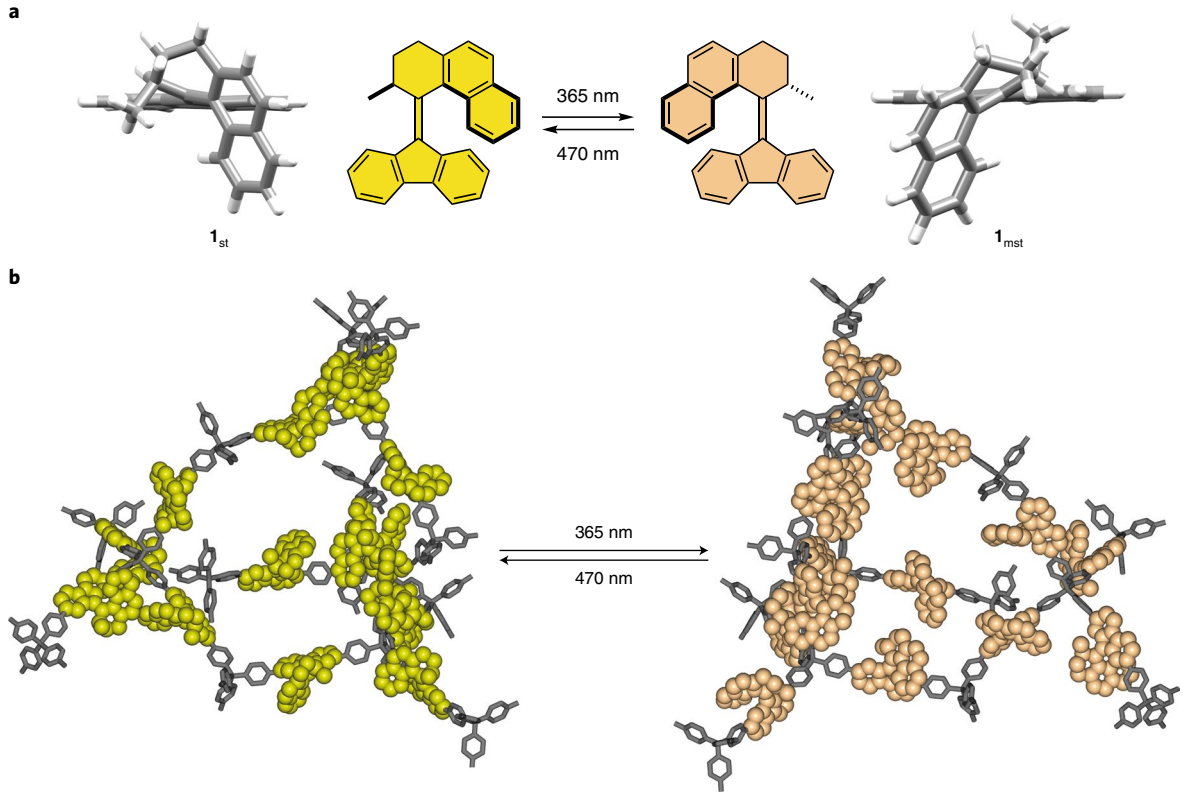

Fig. 1 | Photoisomerization of the overcrowded olefin-based bistable switch. a, Schematic representation of the structural changes on photochemical *E/Z* isomerization of the bistable overcrowded alkene **1** and top view of the DFT (B3LYP/6-31-G(d,p)) optimized structures of the stable ($\mathbf{1}_{st}$, left) and metastable ($\mathbf{1}_{mst}$, right) isomers. **b**, Schematic representation of the photoswitching of the overcrowded alkene **1** in pores of the PSF framework. The stable isomer is yellow and the metastable isomer is beige.

the naphthyl moiety of the photoswitch. The high intrinsic porosity of PSF-type materials alleviates the constraints imposed by a solid environment on the molecular motion and allows for bulk photoisomerization in the solid state as well as photomodulation of the materials porosity. This transformation probably involves a cooperative rearrangement of the flexible, yet constrained, framework and carries the local strain and conformational changes into a conformational restructuring of the framework, which thus enables on-command and non-invasive modulation of the observed porosity.

Results and discussion

Synthesis of PSFs. The fabrication of robust porous materials with the overcrowded alkene-based chiroptical switch $\mathbf{1}_{st}$ directly inserted into the framework through covalent bonds was realized by a Yamamoto cross-coupling reaction. The reaction between a network-forming tridimensional monomer, tetra-*p*-bromo-phenylmethane (TPM-Br_4), and the overcrowded alkene-based chiroptical switch $\mathbf{1}_{st}$-Br_2 that bears two bromide substituents afforded the desired frameworks (Fig. 2a). The choice of the tetraphenylmethane (TPM) building block was motivated by the very high pore capacity and Brunauer–Emmett–Teller surface area up to ~5,000 $m^2 g^{-1}$ of the TPM-based framework[23,62], which we envisaged to be suitable to provide a sufficient free volume for the isomerization of overcrowded alkene **1** embedded in the solid material. Two PSFs were synthesized by varying the molar fraction of the building blocks (TPM and **1**) used during the synthesis of the materials denoted as PSF-1 and PSF-2 (10:1 and 4:1 of TPM-Br_4 to $\mathbf{1}_{st}$-Br_2 for PSF-1 and PSF-2, respectively (for the synthetic details and characterization see Methods and Supplementary Information). The resulting PSFs were stable up to 450 °C, as determined by thermogravimetric analysis (Fig. 2d). The porosity of the materials was established by N_2 adsorption isotherms at 77 K (Fig. 2c). The Langmuir and Brunauer–Emmett–Teller surface areas were as large as 4,545 and 3,948 $m^2 g^{-1}$ for PSF-1 and 1,330 and 1,177 $m^2 g^{-1}$ for PSF-2 with pore capacities of 2.39 and 0.66 $cm^3 g^{-1}$, respectively, and the pore size distribution was centred at about 1.4 nm for PSF-1 and 1.2 nm for PSF-2, as calculated by non-local density functional theory (DFT) (Supplementary Fig. 12 and Supplementary Table 2). The hysteretic loops are indicative of the framework swellability[62–64]. The homogeneity of the samples and the molecular composition of the frameworks were established by elemental analysis (Supplementary Table 1) and quantitative ^{13}C magic angle spinning (MAS) NMR spectroscopy (Fig. 2b and Supplementary Fig. 6): the results correspond to the fractions of the building blocks used in the synthesis of the frameworks. Thus, the fraction of the switch unit in the PSFs can be modulated at will, and PSF-1 and PSF-2 were used for later experiments.

Photochemical and thermal isomerization in solution. The photochemical isomerization behaviour of $\mathbf{1}_{st}$-Br_2 in solution was studied with ^1H and ^{13}C NMR, ultraviolet–visible (UV-vis) absorption and Raman spectroscopies. In the ^1H NMR spectrum, irradiation of $\mathbf{1}_{st}$-Br_2 at 365 nm in CD_2Cl_2 solution resulted in the appearance of a new set of ^1H downfield-shifted resonances, which indicates the formation of the metastable isomer ($\mathbf{1}_{mst}$-Br_2) with almost quantitative yield (photostationary state at 365 nm (PSS_{365}) 94:6 of $\mathbf{1}_{mst}$-Br_2:$\mathbf{1}_{st}$-Br_2) (Fig. 3a; see Methods for details). Likewise, in the ^{13}C NMR spectrum, a new set of upfield-shifted resonances for carbons C_a (35.6 → 34.6 ppm), and C_c (30.0 → 28.5 ppm) was observed,

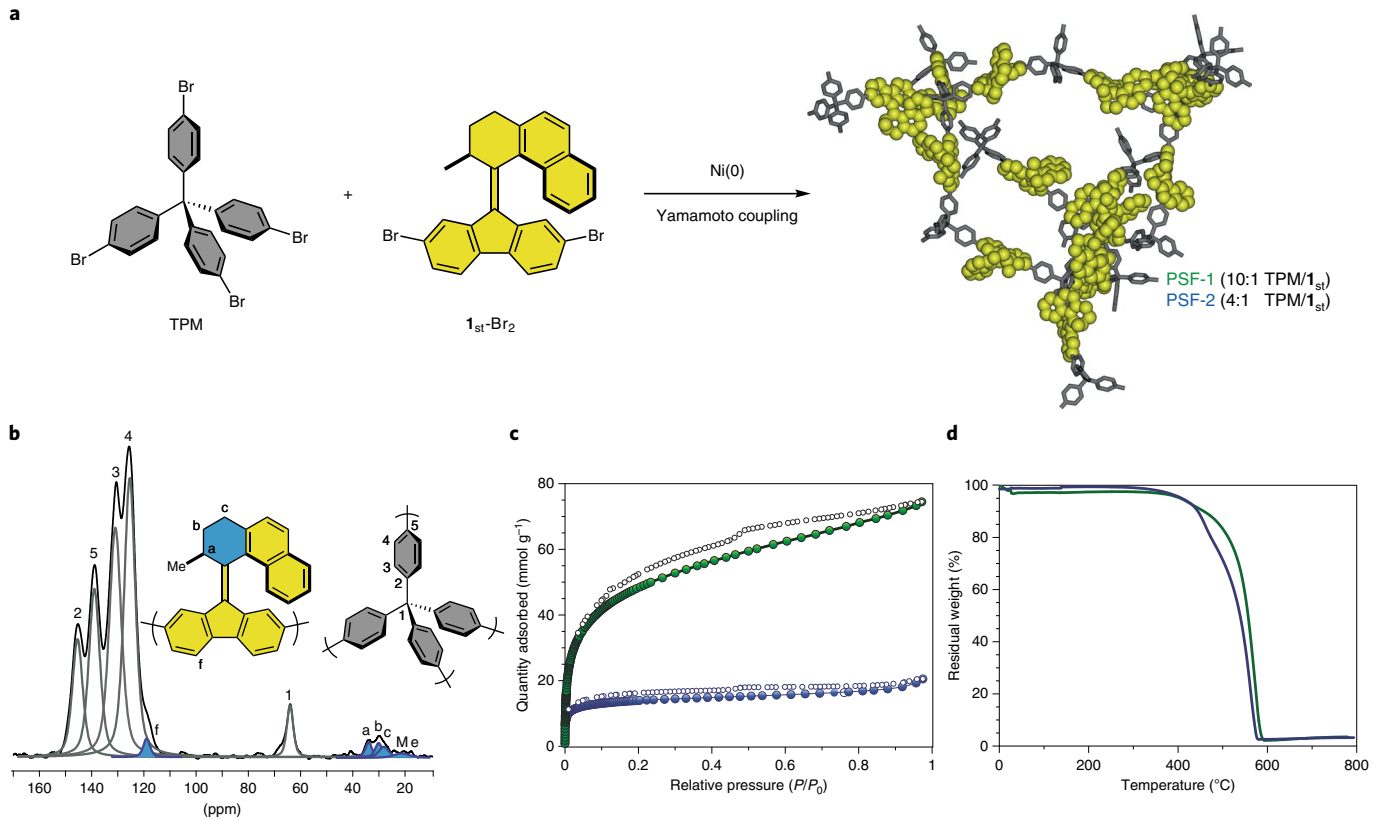

Fig. 2 | Synthesis, structure, sorption and thermal properties of PSF materials. a, Schematic representation of synthesis of the PSF-1 and PSF-2 materials from TPM-Br$_4$ and photoswitch $\mathbf{1}_{st}$-Br$_2$ via Yamamoto coupling. **b**, Solid-state ^{13}C MAS NMR (75.04 MHz, 12.5 kHz, recycle delay = 100 s) spectrum of the PSF-2 material. The peaks highlighted in blue correspond to the cyclohexene ring. **c**, N_2 gas adsorption isotherms (77 K) of activated PSF-1 (green) and PSF-2 (blue). Filled and empty symbols denote adsorption and desorption, respectively. Additional N_2 adsorption isotherms for PSF-2 are shown in Fig. 6. **d**, Thermogravimetric analysis profiles show the stability of PSF-1 (green line) and PSF-2 (blue line) up to 450 °C.

in line with the formation of $\mathbf{1}_{mst}$-Br$_2$ (Fig. 3b). In the UV-vis absorption spectrum, irradiation at 365 nm led to a gradual bathochromic shift of the absorption band centred at 366 nm. This shift of absorption is consistent with the formation of the metastable twisted isomer of the overcrowded alkene-based photoswitch. During the photoisomerization, an isosbestic point was maintained at 385 nm, which indicates a unimolecular process (Fig. 3c). In the Raman spectrum of $\mathbf{1}_{st}$-Br$_2$, a band centred at 1,582 cm^{-1} is present, characteristic of the stretching of the olefinic bond of the photoswitch $\mathbf{1}_{st}$-Br$_2$. On irradiation of the sample at 365 nm, this band disappeared as a new broad band centred at 1,542 cm^{-1}, characteristic of the stretching of the olefinic bond of the metastable overcrowded alkene $\mathbf{1}_{mst}$-Br$_2$, appeared. The reverse $\mathbf{1}_{mst}$-Br$_2$ → $\mathbf{1}_{st}$-Br$_2$ isomerization in solution could be achieved by irradiation of $\mathbf{1}_{mst}$ at 470 nm, on which the ^{1}H NMR resonances of $\mathbf{1}_{st}$-Br$_2$ reappeared (PSS_{470} 97:3 $\mathbf{1}_{st}$-Br$_2$:$\mathbf{1}_{mst}$-Br$_2$) (Supplementary Figs. 2 and 3) and the original UV-vis absorption and Raman spectra were recovered (Fig. 3c,d).

Photochemical isomerization in the solid state. The photochemical isomerization behaviour (Fig. 4a,b) of switch **1** embedded in the solid PSF-1 and PSF-2 frameworks was studied with diffuse-reflectance UV-vis (DR UV-vis) and Raman spectroscopies (Fig. 4c–f). On exposure to light irradiation, spectral changes almost identical to those found in solution were detected for both porous materials (PSF-1 and PSF-2), which indicates a facile photoisomerization of the overcrowded alkene embedded in the PSFs. In the DR UV-vis spectra of PSF-1 and PSF-2, bathochromic shifts were observed on irradiation at 365 nm and hypsochromic shifts on irradiation at 470 nm, in line with the light-reversible $\mathbf{1}_{mst} \leftrightarrow \mathbf{1}_{st}$ photoisomerization (Fig. 4c,d, respectively). Additionally, the evident colour change of the material exposed to 365 nm light was readily visible, which is consistent with the bathochromic shift of the absorption spectra of the material (Fig. 4b). For both materials, the alternating cycles of the ultraviolet and visible light irradiations could be repeated for several cycles without any noticeable sign of fatigue, which indicates the high stability of the material (Fig. 4c,d insets for PSF-1 and PSF-2, respectively). The Raman spectra of both solid PSFs were dominated by an intense broad band centred at 1,610 cm^{-1}, characteristic of the benzene ring stretching mode associated with the relatively large fraction of TPM building blocks in both frameworks. Nevertheless, irradiation of the porous materials at 365 nm resulted in the expected decrease in Raman intensity at 1,582 cm^{-1} and the appearance of a distinctive new band at 1,542 cm^{-1}. Irradiation at 470 nm fully reversed these changes for the PSF-1 framework, as the band characteristic of the $\mathbf{1}_{mst}$ isomer could not be detected in the Raman spectrum, which clearly demonstrates the reversible photoisomerization of **1** incorporated in the solid material (Fig. 4e). Conversely, **1** incorporated in the PSF-2 framework showed only a partial back-isomerization to $\mathbf{1}_{st}$ on irradiation at 470 nm, as indicated by the incomplete disappearance of the band at 1,542 cm^{-1}. Complete reversibility occurred by thermal treatment, as shown below (160 °C for 15 h; see Methods for details).

Solid-state ^{13}C MAS NMR spectroscopy proved to be an invaluable tool to highlight the structural changes that occurred within the individual components of the framework at a molecular level, and thus provides a precise and quantitative measure of the extent of photoisomerization in the material bulk. For the solid-state NMR

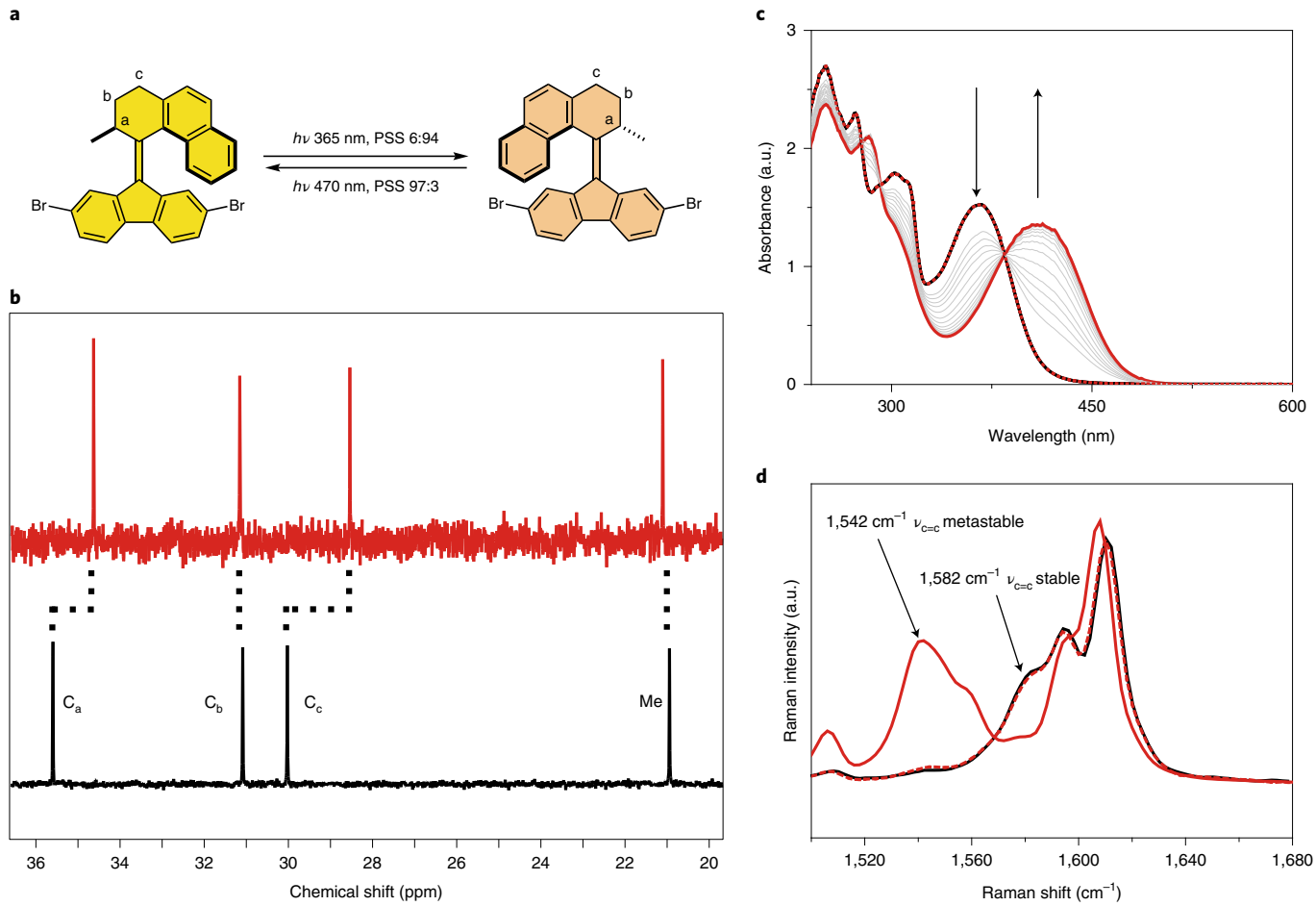

Fig. 3 | Photochemical isomerization of bistable switch 1-Br_2 in solution. a, Schematic representation of the structural change on photochemical *E*/*Z* isomerization of the overcrowded alkene-based bistable switch **1**-Br_2. **b**, Comparison of the aliphatic part of ^{13}C NMR (CD_2Cl_2, 400 MHz, atom labelling as in **a**) spectra of $\mathbf{1}_{st}$-Br_2 (black spectrum) and $\mathbf{1}_{mst}$-Br_2 (as a PSS_{365} mixture obtained on sufficient irradiation at 365 nm; red spectrum). **c**, The changes in the UV-vis absorption spectra of $\mathbf{1}_{st}$-Br_2 (black line) (8 μM, dichloromethane (DCM); black spectrum) on irradiation at 365 nm comprised a large bathochromic shift of the absorption bands characteristic of the metastable isomer (red line), and subsequent irradiation at 470 nm led to the recovery of the initial spectrum (red, dashed line). Grey lines indicate intermediate states and black arrows indicate the direction of spectral changes on irradiation at 365 nm. Note that isosbestic points were maintained throughout isomerizations, which indicates that both isomerizations are unimolecular. **d**, The changes in the Raman spectra (785 nm, 50 mW, solutions drop cast on a quartz substrate) of $\mathbf{1}_{st}$-Br_2 (black line) on irradiation at 365 nm resulted in the appearance of a new broad band at 1,542 cm^{-1}, characteristic of $\mathbf{1}_{mst}$-Br_2 (red continuous line), and subsequent irradiation at 470 nm led to the recovery of $\mathbf{1}_{st}$-Br_2 and the initial spectrum (red dashed line). The bands that correspond to the stretching modes characteristic of metastable (1,542 cm^{-1}) and stable (1,582 cm^{-1}) isomers are indicated. a.u., arbitrary units.

studies, the PSF-2 framework was chosen as a starting point owing to its higher content of photoswitch **1**, which facilitated a quantitative analysis of the spectra. To this end, the PSF-2 material was irradiated at 365 nm with a low power density (~3 mW cm^{-2} for 54 h) and ^{13}C MAS NMR spectra were recorded. On irradiation of PSF-2 at 365 nm, similar changes to those observed in solution were recorded, that is, the upfield shift of the resonances of the carbons C_a (35.0 → 34.1 ppm) and C_c (29.2 → 28.0 ppm) (Fig. 5b). This similarity to the solution studies allowed us to unequivocally ascribe these changes to the photochemical formation of the metastable isomer ($\mathbf{1}_{mst}$) embedded in the framework, in agreement with DR UV-vis and Raman spectral data (Fig. 4). Deconvolution of the spectrum and integration of the resonances that originated from the respective diastereoisomers (Fig. 5b, middle panel, and Supplementary Table 5) showed that the PSS achieved on irradiation of the bulk material (93:7 of $\mathbf{1}_{mst}$:$\mathbf{1}_{st}$) is as high as that in solution (94:6 of $\mathbf{1}_{mst}$:$\mathbf{1}_{st}$). These results are remarkable as quantitative photoswitching of solid materials have been reported only for flexible MOFs that contain dithienylethene-derived struts[42,45] and porous molecular crystals sustained by weak van der Waals interactions[29]. Furthermore, similar quantitative results were obtained for three distinct samples, which thus demonstrates the reproducibility of these data within a small error margin (Supplementary Fig. 16).

On irradiation at 470 nm, the metastable form reverted only partially to the stable form, as determined by solid-state NMR spectroscopy (Supplementary Fig. 17 and Supplementary Table 5) and in accordance with Raman spectroscopy. Conversely, complete reversibility was achieved by thermal treatment: indeed, owing to the noticeable thermal stability, the samples were cured at 160 °C (15 h) and 200 °C (2 h) with the $\mathbf{1}_{mst}$ isomer quantitatively converted back to the $\mathbf{1}_{st}$ isomer, as shown by the recovery of the original ^{13}C MAS NMR spectrum (Fig. 5b, right panel). Accordingly, the PSF-1 material showed the same, nearly quantitative, light- and heat-induced isomerization cycle, which could be followed and quantified by MAS NMR, despite the moderate switch fraction in the framework (Supplementary Figs. 19 and 20). This intriguing trend confirms the

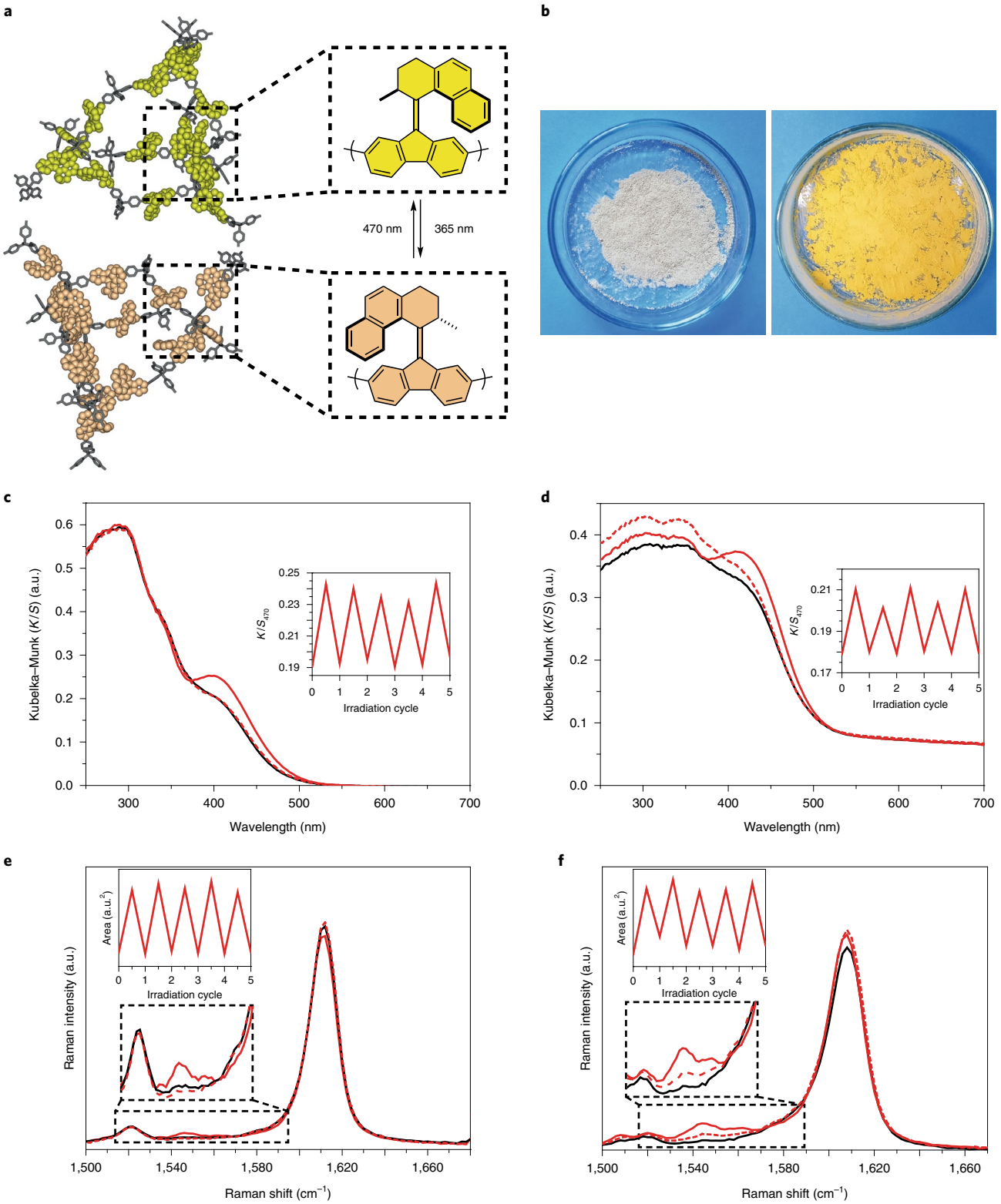

Fig. 4 | Photochemical isomerization studies in the solid state. a, Schematic representation of light-induced structural changes in the PSFs on isomerization of **1** from the stable to the metastable isomer. **b**, Pictures of the PSF-2 material before (left) and after (right) irradiation at 365 nm for 30 min (power density ~20 mW cm^{-2}). **c**,**d**, Changes in the DR UV-vis spectra of the PSF (PSF-1 (**c**) and PSF-2 (**d**)) materials on consecutive irradiation at 365 nm followed by irradiation at 470 nm for 45 min (power density ~8 mW cm^{-2}). The PSS of the pristine materials (black lines), on irradiation at 365 nm (red continuous lines, PSS_{365}) and on subsequent irradiation of the materials at 470 nm (red dashed lines, PSS_{470}). The insets show changes in the Kubelka–Munk (K/S, where K and S denote absorption and scattering coefficients, respectively) function at 470 nm over alternative irradiation cycles. **e**,**f**, Changes in the Raman spectra (785 nm, 50 mW) of the PSF-1 (**e**) and PSF-2 (**f**) materials on irradiation at 365 nm followed by irradiation at 470 nm. The PSS of the pristine materials (black lines), on irradiation at 365 nm (red continuous lines, PSS_{365}) and on subsequent irradiation of the materials at 470 nm (red dashed lines, PSS_{470}). The top-left insets show changes in the area of the band centred at 1,547 cm^{-1} over alternative irradiation cycles. Expansions of the left parts of the spectra are also shown.

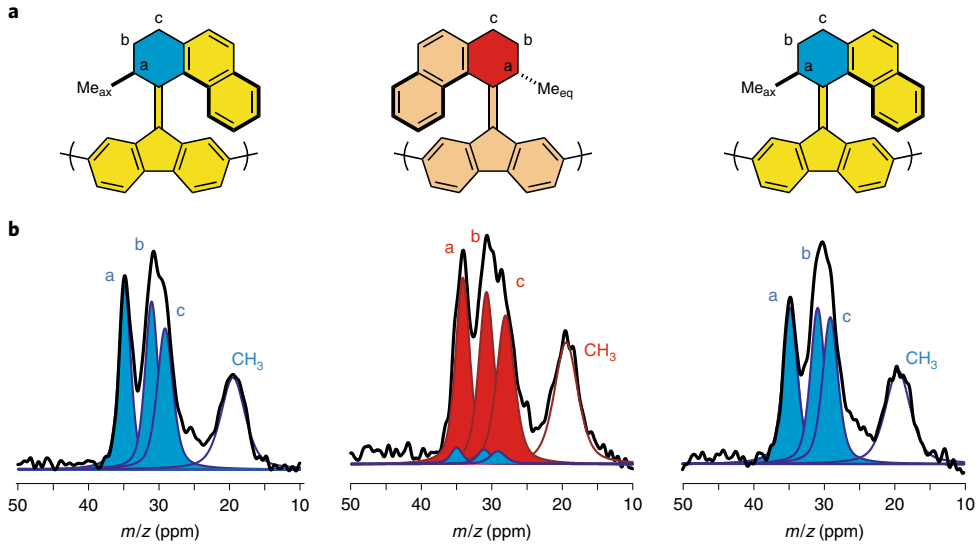

Fig. 5 | Solid-state NMR observations of the reversible structural switching in PSF-2. a, Schematic representation of the structural changes of **1** (**1**$_{st}$) (left) incorporated in the PSF-2 framework on irradiation at 365 nm (**1**$_{mst}$) (middle) and subsequent heating (**1**$_{st}$) (right). **b**, Changes in the $^{13}C\{^1H\}$ cross-polarization MAS NMR spectra of the PSF-2 framework at each stage of the structural transformations, pristine (left), after photoisomerization (middle) and after thermal annealing (right). The cyclohexene ring and the corresponding NMR resonances in the stable isomer are highlighted in blue and those in the metastable isomer are highlighted in red. After photoisomerization, a minor amount of the stable state was detected, as indicated by the blue peaks in the middle spectrum. ax, axial; eq, equatorial.

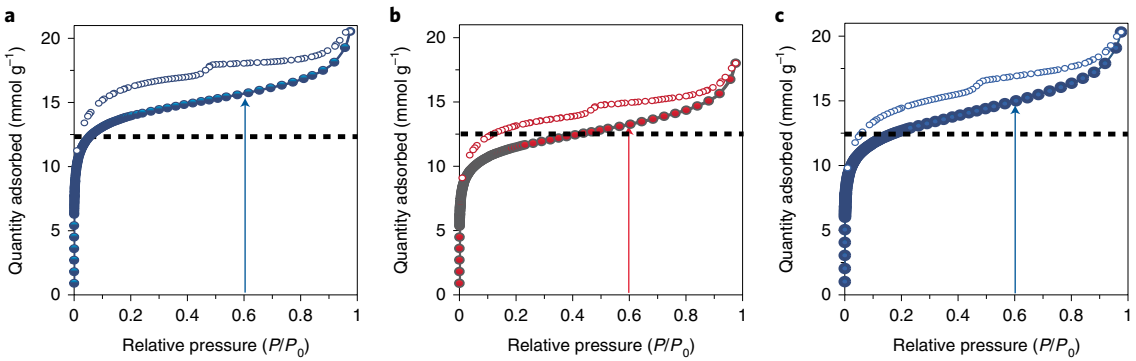

Fig. 6 | Switching of the gas adsorption properties. a,**b**, N_2 adsorption isotherms of the PSF-2 framework at 77 K for the pristine material (**a**, blue), after irradiation at 365 nm for 54 h (**b**, red) and heating (**c**, blue). The filled and open circles denote adsorption and desorption isotherms, respectively. The arrows indicate the adsorbed gas amount at $P/P_0 = 0.6$. The isotherm of the pristine material is an enlargement of the isotherm reported in Fig. 2c.

virtually unhindered confinement in which the switch function was preserved by insertion in the low-density framework.

Gas adsorption experiments. We anticipated that the accessible volume of the framework would be reversibly changed during the overall stable–metastable–stable isomerization sequence and, therefore, gas adsorption experiments were performed. Indeed, N_2 adsorption isotherms at 77 K revealed a striking reduction in the pore volume between pristine and irradiated PSF-2 materials, which accounts for 20% at a relative pressure (P/P_0) of 0.6 (Fig. 6). Furthermore, this phenomenon was nearly fully reversible after heating of the irradiated material, as demonstrated by the N_2 adsorption isotherm (Fig. 6c and Supplementary Table 3). Conversely, only a partial recovery of the surface area (approximately 40% of the initial value) was observed for the PSF-2 material on prolonged irradiation at 470 nm, in line with the incomplete reverse isomerization of the **1**$_{mst}$ to **1**$_{st}$ under these conditions, as determined by solid-state NMR spectroscopy (Supplementary Figs. 17 and 18). In addition, the light- and heat-induced switching cycle of PSF-1 yielded N_2 adsorption isotherm behaviour consistent with that of PSF-2, although a smaller reduction was observed, in line with the lower switch concentration and the larger pore volume of the sample (Supplementary Fig. 19). The 20% reduction of pore volume on PSF-2 irradiated at 365 nm was corroborated by CO_2 adsorption isotherms at 195 K (from 500 to 402 cm^3 g^{-1} (STP); Supplementary Fig. 13). This decrease in the adsorption capacity on irradiation of almost 100 cm^3 g^{-1} (STP) is a benchmark and exceeds the values so far reported of ~33 cm^3 g^{-1} (STP) for the dithienylethene-based MOF[45] and 52 cm^3 g^{-1} (STP) for the porous star-shaped azobenzene tetramer molecular crystal[29], and is comparable to the value of the MOF with azobenzene pendants[65]. The similar relative drops in adsorption for both probe gases (approximately 20% for N_2 and for CO_2) and negligible changes in the dipole moment of the switch **1** on photoisomerization (Supplementary Fig. 20) indicate that the electrostatic interactions do not play a dominant role in the change of sorption capacity of the PSF-2 framework[65,66]. Indeed, the CO_2 adsorption isotherms at various temperatures (273, 283 and 298 K; Supplementary Fig. 14) analysed by the van't Hoff equation gave

isosteric heats of adsorption at low coverage of 27.1 and 27.9 kJ mol^{-1} at 0.2 mmol g^{-1} for PSF-2 with $\mathbf{1}_{st}$ and $\mathbf{1}_{mst}$, respectively, which indicates that the frameworks exhibit similar interactions with CO_2. Hence, the differences in the observed porosity of the material on isomerization of **1** most probably originate from structural changes of the switch and the framework on photoisomerization. The structures and geometries of both the stable and metastable isomers were optimized by DFT on the B3LYP 6-31 G(d,p) level of theory. Although the stable isomer adopts a folded conformation in which both methyl and naphthyl substituents are located on the same side of the central olefinic bond, the steric congestion in the metastable isomer forces the molecule to adopt a twisted conformation. As a result, the dihedral angles between substituents of the central double bond increase from 13.4 and 14.4° in $\mathbf{1}_{st}$ to 25.2 and 27.3° for $\mathbf{1}_{mst}$. When the switch is inserted covalently in the framework, it bears two *p*-phenyl substituents, which belong to the TPM unit and interact with naphthyl moiety at shorter distances in the stable than in the metastable configuration (Supplementary Fig. 21). Owing to the flexibility and hyper-cross-linked nature of the 3D framework, the differential local interactions between the switch and the comonomeric unit presumably trigger an extensive rearrangement of the architecture, which generates the remarkable impact on the pore volume and the gas uptake.

Conclusions

In summary, we developed a successful strategy to fabricate light-responsive porous materials in which overcrowded alkene-based photoswitches are covalently incorporated into a solid and robust framework. Our approach realizes a continuous covalent framework by a copolymerization process that involves the functionalized switch and a comonomer, which sustains the architecture and promotes porosity. Two PSFs that consisted of a TPM moiety and various amounts of photoswitch were obtained by the formation of carbon–carbon bonds, such that the switch is an intrinsic part of the framework itself. The great stability of the solid-state framework, combined with the dynamics of the light-responsive switches, were proved to modulate the gas sorption, and yet retain a high porosity in each respective geometry. Such a high porosity for both states of the bistable switch provided by our strategy was crucial to achieve the unhindered reversible photoisomerization in the solid state. The proposed synthetic strategy is simple and straightforward, yet it guarantees the full incorporation of the light-responsive switch as a functional component in a controlled amount with respect to a pore-forming unit. By the combination of DR UV-vis and Raman spectroscopies, it was demonstrated that the chiroptical switch embedded in the porous framework maintained its function and can undergo wavelength-dependent isomerization on exposure to light. Furthermore, solid-state NMR studies performed on the framework with a higher photoswitch content showed that the PSS ratio of the chiroptical switch **1** inserted in the framework, as established in the solid sample on exposure to ultraviolet irradiation, is essentially the same as that reached in solution. These findings are highly remarkable because the values of PPS previously reported for bulk solid materials were not as high as those in solution. Furthermore, the porosity and gas uptake of the porous switch frameworks can be reversibly modulated with light and heat owing to the unique quantitative photoisomerization in the bulk of the porous material. Also, these extensive aromatic frameworks entail an exceptional thermal and chemical stability, which make them usable for many cycles. The novel prototypical materials allow us to envision the generation of responsive properties of practical utility, such as the regulation of adsorption on command. Our findings also open up opportunities to design responsive porous organic frameworks that contain rotors, motors and switches, and so exhibit specialized functions beyond a controlled gas uptake and release, such as switchable size-based or enantiomer-based[67] separation technologies.

Online content

Any methods, additional references, Nature Research reporting summaries, source data, extended data, supplementary information, acknowledgements, peer review information; details of author contributions and competing interests; and statements of data and code availability are available at https://doi.org/10.1038/s41557-020-0493-5.

Received: 16 August 2019; Accepted: 27 May 2020;
Published online: 26 June 2020

References

1. Dietrich-Buchecker, C., Jimenez-Molero, M. C., Sartor, V. & Sauvage, J.-P. Rotaxanes and catenanes as prototypes of molecular machines and motors. *Pure Appl. Chem.* **75**, 1383–1393 (2003).
2. Balzani, V., Venturi, M. & Credi, A. *Molecular Devices and Machines: A Journey into the Nano World*. (Wiley, 2003).
3. Kay, E. R., Leigh, D. A. & Zerbetto, F. Synthetic molecular motors and mechanical machines. *Angew. Chem. Int. Ed.* **46**, 72–191 (2007).
4. Erbas-Cakmak, S., Leigh, D. A., McTernan, C. T. & Nussbaumer, A. L. Artificial molecular machines. *Chem. Rev.* **115**, 10081–10206 (2015).
5. Browne, W. R. & Feringa, B. L. Making molecular machines work. *Nat. Nanotechnol.* **1**, 25–35 (2006).
6. Kinbara, K. & Aida, T. Toward intelligent molecular machines: directed motions of biological and artificial molecules and assemblies. *Chem. Rev.* **105**, 1377–1400 (2005).
7. Astumian, R. D., Kay, E. R., Leigh, D. A. & Zerbetto, F. Design principles for Brownian molecular machines: how to swim in molasses and walk in a hurricane. *Proc. Natl Acad. Sci. USA* **46**, 10771–10776 (2006).
8. Coskun, A., Banaszak, M., Astumian, R. D., Stoddart, J. F. & Grzybowski, B. A. Great expectations: can artificial molecular machines deliver on their promise? *Chem. Soc. Rev.* **41**, 19–30 (2012).
9. Astumian, R. D. How molecular motors work–insights from the molecular machinist's toolbox: the Nobel Prize in Chemistry 2016. *Chem. Sci.* **8**, 840–845 (2017).
10. van Leeuwen, T., Lubbe, A. S., Štacko, P., Wezenberg, S. J. & Feringa, B. L. Dynamic control of function by light-driven molecular motors. *Nat. Rev. Chem.* **1**, 0096 (2017).
11. Furukawa, H., Cordova, K. E., O'Keeffe, M. & Yaghi, O. M. The chemistry and applications of metal–organic frameworks. *Science* **341**, 1230444 (2013).
12. Howarth, A. J. et al. Chemical, thermal and mechanical stabilities of metal–organic frameworks. *Nat. Rev. Mater.* **1**, 1–15 (2016).
13. Kitagawa, S., Kitaura, R. & Noro, S. Functional porous coordination polymers. *Angew. Chem. Int. Ed.* **43**, 2334–2375 (2004).
14. Diercks, C. S. & Yaghi, O. M. The atom, the molecule, and the covalent organic framework. *Science* **355**, eaal1585 (2017).
15. Das, S., Heasman, P., Ben, T. & Qiu, S. Porous organic materials: strategic design and structure–function correlation. *Chem. Rev.* **117**, 1515–1563 (2017).
16. Gould, S. L., Tranchemontagne, D., Yaghi, O. M. & Garcia-Garibay, M. A. The amphidynamic character of crystalline MOF-5: rotational dynamics in a free-volume environment. *J. Am. Chem. Soc.* **130**, 3246–3247 (2008).
17. Vogelsberg, C. S. et al. Ultrafast rotation in an amphidynamic crystalline metal organic framework. *Proc. Natl Acad. Sci. USA* **114**, 13613–13618 (2017).
18. Comotti, A., Bracco, S. & Sozzani, P. Molecular rotors built in porous materials. *Acc. Chem. Res.* **49**, 1701–1710 (2016).
19. Bracco, S. et al. CO_2 regulates molecular rotor dynamics in porous materials. *Chem. Commun.* **53**, 7776–7779 (2017).
20. Bracco, S. et al. Ultrafast molecular rotors and their CO_2 tuning in MOFs with rod-like ligands. *Chem. Eur. J.* **23**, 11210–11215 (2017).
21. Vukotic, V. N., Harris, K. J., Zhu, K., Schurko, R. W. & Loeb, S. J. Metal–organic frameworks with dynamic interlocked components. *Nat. Chem.* **4**, 456–460 (2012).
22. Vukotic, V. N. et al. Mechanically interlocked linkers inside metal–organic frameworks: effect of ring size on rotational dynamics. *J. Am. Chem. Soc.* **137**, 9643–9651 (2015).
23. Comotti, A., Bracco, S., Ben, T., Qiu, S. & Sozzani, P. Molecular rotors in porous organic frameworks. *Angew. Chem. Int. Ed.* **53**, 1043–1047 (2014).
24. Zhu, K., O'Keefe, C. A., Vukotic, V. N., Schurko, R. W. & Loeb, S. J. A molecular shuttle that operates inside a metal–organic framework. *Nat. Chem.* **7**, 514–519 (2015).
25. Chen, Q. et al. A redox-active bistable molecular switch mounted inside a metal–organic framework. *J. Am. Chem. Soc.* **138**, 14242–14245 (2016).
26. Danowski, W. et al. Unidirectional rotary motion in a metal–organic framework. *Nat. Nanotechnol.* **14**, 488–494 (2019).
27. Coudert, F. X. Responsive metal–organic frameworks and framework materials: under pressure, taking the heat, in the spotlight, with friends. *Chem. Mater.* **27**, 1905–1916 (2015).

28. Castellanos, S., Kapteijn, F. & Gascon, J. Photoswitchable metal organic frameworks: turn on the lights and close the windows. *CrystEngComm* **18**, 4006–4012 (2016).
29. Baranconi, M. et al. Photoinduced reversible switching of porosity in molecular crystals based on star-shaped azobenzene tetramers. *Nat. Chem.* **7**, 634–640 (2015).
30. Wang, Z. et al. Series of photoswitchable azobenzene-containing metal–organic frameworks with variable adsorption switching effect. *J. Phys. Chem. C* **122**, 19044–19050 (2018).
31. Prasetya, N., Donose, B. C. & Ladewig, B. P. A new and highly robust light-responsive Azo-UiO-66 for highly selective and low energy post-combustion CO_2 capture and its application in a mixed matrix membrane for CO_2/N_2 separation. *J. Mater. Chem. A* **6**, 16390–16402 (2018).
32. Castellanos, S. et al. Structural effects in visible-light-responsive metal–organic frameworks incorporating *ortho*-fluoroazobenzenes. *Chem. Eur. J.* **22**, 746–752 (2016).
33. Brown, J. W. et al. Photophysical pore control in an azobenzene-containing metal–organic framework. *Chem. Sci.* **4**, 2858–2864 (2013).
34. Gong, L. L., Feng, X. F. & Luo, F. Novel azo–metal–organic framework showing a 10-connected bct net, breathing behavior, and unique photoswitching behavior toward CO_2. *Inorg. Chem.* **54**, 11587–11589 (2015).
35. Heinke, L. et al. Photoswitching in two-component surface-mounted metal–organic frameworks: optically triggered release from a molecular container. *ACS Nano* **8**, 1463–1467 (2014).
36. Lyndon, R. et al. Dynamic photo-switching in metal–organic frameworks as a route to low-energy carbon dioxide capture and release. *Angew. Chem. Int. Ed.* **52**, 3695–3698 (2013).
37. Wang, Z. et al. Tunable molecular separation by nanoporous membranes. *Nat. Commun.* **7**, 13872 (2016).
38. Yu, X. et al. *Cis*-to-*trans* isomerization of azobenzene investigated by using thin films of metal–organic frameworks. *Phys. Chem. Chem. Phys.* **17**, 22721–22725 (2015).
39. Park, J. et al. Reversible alteration of CO_2 adsorption upon photochemical or thermal treatment in a metal–organic framework. *J. Am. Chem. Soc.* **134**, 99–102 (2012).
40. Walton, I. M. et al. Photo-responsive MOFs: light-induced switching of porous single crystals containing a photochromic diarylethene. *Chem. Commun.* **49**, 8012–8014 (2013).
41. Patel, D. G. et al. Photoresponsive porous materials: the design and synthesis of photochromic diarylethene-based linkers and a metal–organic framework. *Chem. Commun.* **50**, 2653–2656 (2014).
42. Nikolayenko, V. I., Herbert, S. A. & Barbour, L. J. Reversible structural switching of a metal–organic framework by photoirradiation. *Chem. Commun.* **53**, 11142–11145 (2017).
43. Fan, C. B. et al. Significant enhancement of C_2H_2/C_2H_4 separation by a photochromic diarylethene unit: a temperature- and light-responsive separation switch. *Angew. Chem. Int. Ed.* **56**, 7900–7906 (2017).
44. Luo, F. et al. Photoswitching CO_2 capture and release in a photochromic diarylethene metal–organic framework. *Angew. Chem. Int. Ed.* **53**, 9298–9301 (2014).
45. Zheng, Y. et al. Flexible interlocked porous frameworks allow quantitative photoisomerization in a crystalline solid. *Nat. Commun.* **8**, 100 (2017).
46. Williams, D. E. et al. Energy transfer on demand: photoswitch-directed behavior of metal–porphyrin frameworks. *J. Am. Chem. Soc.* **136**, 11886–11889 (2014).
47. Furlong, B. J. & Katz, M. J. Bistable dithienylethene-based metal–organic framework illustrating optically induced changes in chemical separations. *J. Am. Chem. Soc.* **139**, 13280–13283 (2017).
48. Irie, M., Fukaminato, T., Matsuda, K. & Kobatake, S. Photochromism of diarylethene molecules and crystals: memories, switches, and actuators. *Chem. Rev.* **114**, 12174–12277 (2014).
49. Kolokolov, D. I. et al. Flipping the switch: fast photoisomerization in a confined environment. *J. Am. Chem. Soc.* **140**, 7611–7622 (2018).
50. Dolgopolova, E. A. et al. Connecting wires: photoinduced electronic structure modulation in metal–organic frameworks. *J. Am. Chem. Soc.* **141**, 5350–5358 (2019).
51. Kundu, P. K., Olsen, G. L., Kiss, V. & Klajn, R. Nanoporous frameworks exhibiting multiple stimuli responsiveness. *Nat. Commun.* **5**, 3588 (2014).
52. Koumura, N., Zijistra, R. W. J., van Delden, R. A., Harada, N. & Feringa, B. L. Light-driven monodirectional molecular rotor. *Nature* **401**, 152–155 (1999).
53. Koumura, N., Geertsema, E. M., Meetsma, A. & Feringa, B. L. Light-driven molecular rotor: unidirectional rotation controlled by a single stereogenic center. *J. Am. Chem. Soc.* **122**, 12005–12006 (2000).
54. Kistemaker, J. C. M., Pizzolato, S. F., van Leeuwen, T., Pijper, T. C. & Feringa, B. L. Spectroscopic and theoretical identification of two thermal isomerization pathways for bistable chiral overcrowded alkenes. *Chem. Eur. J.* **22**, 13478–13487 (2016).
55. Iamsaard, S. et al. Conversion of light into macroscopic helical motion. *Nat. Chem.* **6**, 229–235 (2014).
56. Orlova, T. et al. Revolving supramolecular chiral structures powered by light in nanomotor-doped liquid crystals. *Nat. Nanotechnol.* **13**, 304–308 (2018).
57. Eelkema, R. et al. Nanomotor rotates microscale objects. *Nature* **440**, 163 (2006).
58. Chen, J. et al. Artificial muscle-like function from hierarchical supramolecular assembly of photoresponsive molecular motors. *Nat. Chem.* **10**, 132–138 (2018).
59. Li, Q. et al. Macroscopic contraction of a gel induced by the integrated motion of light-driven molecular motors. *Nat. Nanotechnol.* **10**, 161–165 (2015).
60. Foy, J. T. et al. Dual-light control of nanomachines that integrate motor and modulator subunits. *Nat. Nanotechnol.* **12**, 540–545 (2017).
61. Chen, K. Y. et al. Control of surface wettability using tripodal light-activated molecular motors. *J. Am. Chem. Soc.* **136**, 3219–3224 (2014).
62. Ben, T. et al. Targeted synthesis of a porous aromatic framework with high stability and exceptionally high surface area. *Angew. Chem. Int. Ed.* **48**, 9457–9460 (2009).
63. Wilson, C. et al. Swellable functional hypercrosslinked polymer networks for the uptake of chemical warfare agents. *Polym. Chem.* **8**, 1914–1922 (2017).
64. Bracco, S. et al. Porous 3D polymers for high pressure methane storage and carbon dioxide capture. *J. Mater. Chem. A* **5**, 10328–10337 (2017).
65. Huang, H., Sato, H. & Aida, T. Crystalline nanochannels with pendant azobenzene groups: steric or polar effects on gas adsorption and diffusion? *J. Am. Chem. Soc.* **139**, 8784–8787 (2017).
66. Huang, R., Hill, M. R., Babarao, R. & Medhekar, N. V. CO_2 adsorption in azobenzene functionalized stimuli responsive metal–organic frameworks. *J. Phys. Chem. C* **120**, 16658–16667 (2016).
67. Shimomura, K., Ikai, T., Kanoh, S., Yashima, E. & Maeda, K. Switchable enantioseparation based on macromolecular memory of a helical polyacetylene in the solid state. *Nat. Chem.* **6**, 429–434 (2014).

Methods

Synthesis of 4-(2,7-dibromo-9H-fluoren-9-ylidene)-3-methyl-1,2,3,4-tetrahydrophenanthrene. A two-neck round-bottom flask equipped with reflux condenser was charged with 2,7-dibromofluorenone **3** (340 mg, 1.0 mmol, 1.0 equiv.) to which Lawesson's reagent (814 mg, 2.0 mmol, 2.0 equiv.) and dry toluene (20 ml) were added and the reaction mixture was heated at 100 °C for 2 h. Next, the reaction mixture was cooled to room temperature, filtrated over a plug of cotton, concentrated in vacuo and the residue purified by column chromatography (SiO_2, pentane/DCM 5:1) and concentrated in vacuo to afford thioketone **4** (Supplementary Scheme 1) as a brown oil (135 mg, 0.38 mmol, 38%), which was used immediately in the next step. A separate flask was charged with hydrazone **2** (85 mg, 0.38 mmol, 1.00 equiv.) and DMF (5 ml) was added. Next, the reaction mixture was cooled to −40 °C, and a solution of [bis(trifluoroacetoxy)iodo]benzene (172 mg, 0.40 mmol, 1.05 eq.) in DMF (2 ml) was added dropwise. The reaction mixture was stirred at −40 °C for 5 min during which the colour of the reaction mixture changed to pink. Next, the solution of the previously prepared thioketone **4** in DCM (10 ml) was added dropwise. The reaction mixture was allowed to warm up to room temperature overnight, and tris(dimethylamino)phosphine (186 mg, 1.14 mmol, 207 µl, 3.00 equiv.) was added and stirring was continued at room temperature for 24 h. Next, the reaction mixture was diluted with EtOAc (60 ml), washed twice with water (2 × 30 ml) and brine (30 ml), dried over $MgSO_4$, filtrated and concentrated in vacuo. The crude product was purified by flash column chromatography (SiO_2, pentane/DCM) to afford **1** as a yellow solid (133 mg, 0.26 mmol, 68%). ^{1}H NMR (400 MHz, $CDCl_3$) δ 8.19 (d, J = 1.6 Hz, 1H), 7.92 (dd, J = 12.3, 8.2 Hz, 2H), 7.79 (d, J = 8.5 Hz, 1H), 7.63 (d, J = 8.1 Hz, 1H), 7.54 (dd, J = 8.1, 1.7 Hz, 1H), 7.52–7.36 (m, 3H), 7.26–7.21 (m, 1H), 7.17 (dd, J = 8.1, 1.8 Hz, 1H), 5.96 (d, J = 1.7 Hz, 1H), 4.20 (p, J = 7.0 Hz, 1H), 2.87–2.74 (m, 1H), 2.66–2.40 (m, 2H), 1.36–1.12 (m, 4H). ^{13}C NMR (101 MHz, $CDCl_3$) δ 147.7, 140.0, 139.4, 139.1, 138.4, 137.0, 132.2, 132.1, 131.6, 131.2, 130.0, 129.5, 129.2, 128.3, 128.1, 127.9, 127.0, 125.7, 125.0, 124.2, 120.9, 120.7, 120.4, 119.8, 34.8, 30.4, 29.4, 20.5. HRMS (ESI positive) calcd $C_{28}H_{20}Br_2$ [M$^+$] 516.9926, found 519.9921.

Synthesis of PSFs. 1 (32.4 mg, 0.063 mmol) and **5** (400 mg, 0.63 mmol) (Supplementary Scheme 1) were transferred in an oven-dried 50-ml two-neck round-bottom flask. The flask was closed with a silicon septum and three vacuum–N_2 cycles were performed. Then, dry THF (30 ml) was transferred by means of a syringe and the mixture was stirred at room temperature (r.t.) under N_2 until complete dissolution of the solids. Meanwhile, inside a glove box, Ni(COD)$_2$ (COD, cyclooctadiene) (1 g, 3.64 mmol) and 2,2′-bipyridyl (570 mg, 3.65 mmol) were transferred to an oven-dried 250-ml three-neck flask equipped with a N_2 inlet. One of the necks was sealed with a silicon septum. The closed flask was brought outside the glove box, covered with aluminium foil and quickly put under fluxing N_2. Then, dry DMF (90 ml), dry THF (20 ml) and COD (0.5 ml, 4.08 mmol) were added by means of a syringe. The violet mixture was stirred at r.t. for a few seconds before it was cooled to 0 °C with an ice bath. As the mixture was cooling down, an oven-dried 50-ml pressure-equilibrating dropping funnel was mounted on the last neck of the flask, flushed with N_2 and finally sealed with a rubber septum. The solution of **1** and **5** previously prepared was transferred to the dropping funnel by means of a syringe and added to the violet mixture over 15–20 min. At the end of the addition, the resulting mixture was stirred at 0 °C for an additional 15 min, then allowed to cool to r.t. and left to react under N_2 for 48 h. Subsequently, the flask was opened to air and diluted aqueous HCl was added (10 ml, 2.5 wt%); the mixture was stirred at r.t. until it turned a bright blue colour. At this point, the suspended white solid was recovered by filtration and washed with THF (2 × 30 ml), water (3 × 30 ml), chloroform (2 × 30 ml) and acetone (2 × 30 ml). PSF-1 was obtained as a pale yellow powder (156 mg, 70 % yield). PSF-2 was synthesized following the same procedure described for PSF-1. The quantities used for PSF-2 were: **1** (75 mg, 0.145 mmol), **5** (370 mg, 0.581 mmol), Ni(COD)$_2$ (1 g, 3.64 mmol), COD (0.5 ml, 4.08 mmol), 2,2′-bipyridyl (570 mg, 3.65 mmol), DMF (90 ml), THF (20 + 30 ml). PSF-2 was obtained as a deep yellow powder (183.6 mg, 78%).

UV-vis absorption and reflectance spectroscopy. Solution UV-vis absorption spectra were collected on a Hewlett-Packard 8453 diode array spectrometer in a 1-cm quartz cuvette. A **1**-Br_2 solution (8 µM, DCM) was irradiated at 365 nm for 10 min until no further changes were observed (that is, PSS_{365} was reached). Next, the PSS_{365} mixture was irradiated at 470 nm for 20 min until no further changes were observed in the UV-vis spectrum. Throughout the irradiation experiments, an isosbestic point was maintained at 385 nm. Solid-state DR UV-vis spectra were collected on a Jasco V-570 UV-vis near-infrared spectrophotometer equipped with a Jasco ISN-470 integrating sphere. Prior to the measurements, the samples of either PSF-1 or PSF-2 (2 mg) were ground with a pestle in a mortar with $BaSO_4$ (100 mg). The resulting samples were put on the sample holder with a quartz window and the spectra were collected. Samples were irradiated at either 365 nm or 470 nm for 5 min with light-emitting diodes (LEDs) placed 10 cm from the sample holder window.

Raman spectroscopy. Raman spectra were collected on a Perkin Elmer Raman Station connected to an Olympus BX51M microscope equipped with a 785-nm 50-mW laser. For solution studies, samples of either **1**-Br_2 or **1**-Br_2-PSS_{365} were drop cast from a DCM solution (10^{-3} M) onto a quartz slide and the Raman spectra were recorded. For PSF-1 or PSF-2, samples were placed on a quartz substrate and irradiated at 365 nm and subsequently 470 nm and the Raman spectra were recorded.

NMR spectroscopy in solution. For ^{13}C and ^{1}H NMR spectra of both PSS_{365} and PSS_{470} mixtures a sample of **1**-Br_2 (10 mM, DCM-d_2) was irradiated at 365 nm for 30 min at r.t. and the spectra were recorded. Subsequently, the same sample was irradiated at 470 nm for 1 h to reach PSS_{470}.

Infrared spectroscopy. Attenuated total reflectance (ATR) Fourier transform infrared spectroscopy was performed on a PerkinElmer FT-IR Nexus spectrometer in the range 400–4,000 cm^{-1}. Compound **1**-Br_2 was drop cast from a 10^{-3} M solution in DCM directly onto the ATR crystal. Compound **1**-Br_2-PSS_{365} was obtained by irradiation of a 10^{-3} M solution at 365 nm for 20 min, and then the sample was drop cast onto the ATR crystal and analysed. PSF-1 and PSF-2 were irradiated as they deposited on the ATR crystal, and then spectra of PSF-1-PSS_{365} and PSF-2-PSS_{365} were collected.

Solid-state NMR spectroscopy. ^{13}C MAS NMR experiments were carried out at 75.5 MHz with a Bruker Avance 300 instrument operated at a static field of 7.04 T and equipped with high-power amplifiers (1 kW) and a 4 mm double resonance MAS probe. ^{13}C{^{1}H} NMR ramped-amplitude cross-polarization experiments were performed at a spinning speed of 12.5 kHz using a contact time of 2 ms, a 90° pulse for a proton of 2.9 µs and a recycle delay of 5 s. Spectral profiles, recorded with 30,840 scans, were simulated by mixed Gaussian/Lorentzian line shapes in the ratio of 0.5:0.5. Quantitative ^{13}C single-pulse excitations MAS NMR experiments were performed at a spinning speed of 12.5 kHz with a recycle delay of 100 s and a 90° pulse of length 3.6 µs. The simulation analyses could provide the quantification of the TPM (78%) and switch (22%) units in the PSF-2 architecture and of the TPM (89%) and switch (11%) in PSF-1, in agreement with the synthetic procedure. Crystalline polyethylene was taken as an external reference at 32.8 ppm relative to tetramethylsilane.

N_2 and CO_2 sorption isotherms at 77 K. N_2 adsorption/desorption isotherms were collected at a liquid N_2 temperature (77 K), whereas CO_2 adsorption/desorption isotherms were carried out at a solid CO_2 temperature (195 K), 273, 283 and 298 K and up to 1 bar by means of a Micromeritics ASAP 2020 HD analyser. All the samples were degassed by heating at 130 °C for 5 h under vacuum (~10^{-3} mmHg) before carrying out the analysis. Specific surface area values were calculated from the N_2 isotherms using the Brunauer–Emmett–Teller and Langmuir models. Pore-size distributions were calculated from N_2 adsorption curves considering a slit-pore geometry and non-local DFT. The isosteric heat of adsorption was calculated by applying the van 't Hoff equation.

Irradiation procedure in the solid state. Irradiation experiments for solid-state NMR and gas adsorption analyses were performed using a Spectroline ENF-20C/FE lamp (6 W) for a 365 nm irradiation and a homemade LED lamp built with nine LEDs (3 W each) for a 470 nm irradiation. About 40 mg of the sample were distributed over a Petri dish (Ø = 4 cm) and thoroughly mixed every 60 min. The lamps were set at approximately 3 cm from the sample. The PSF-2 material was irradiated for 54 h at 365 nm and 72 h at 470 nm, whereas the PSF-1 material was irradiated for 74 h at 365 nm. Heat-promoted back-switching experiments were performed by heating the samples at 200 or 160 °C for 15 h under vacuum by means of a Buchi B-585 glass oven.

Data availability

The data associated with the reported findings are available in the manuscript or the Supplementary Information. Other related data are available from the corresponding author upon request.

Acknowledgements

This work was supported financially by the Netherlands Organization for Scientific Research (NWO-CW), the European Research Council (ERC, advanced grant no. 694345 to B.L.F.), the Ministry of Education, Culture and Science (Gravitation Program no. 024.001.035). We thank the University of Groningen for access to the Peregrine Computing Cluster. A.C. and P.S. acknowledge Ministero dell'Istruzione, dell'Università e della Ricerca (MIUR—Progetto Dipartimento di Eccellenza 2018-2022), PRIN 2015CTEBBA and PRIN 20173L7W8K (NEMO) for financial support. We thank C. X. Bezuidenhout for conformational analysis.

Author contributions

W.D., F.C., S.J.W., P.S. and B.L.F. conceived the project. W.D. synthesized the bistable switch **1**-Br_2 and F.C. synthesized the PSF materials. W.D. performed photoisomerization studies in solution, and Raman and DR UV-vis studies of the PSFs. J.P. performed gas adsorption isotherms and the evaluation of adsorption energy. S.B. and A.C. performed solid-state NMR studies on the synthesized materials. F.C. performed differential scanning calorimetry, thermogravimetric analysis and gas-uptake experiments. W.D.

performed DFT studies. S.J.W., A.C. and B.L.F. guided the project. W.D., A.C., S.J.W., P.S. and B.L.F. wrote the manuscript. All the authors discussed the results and commented on the manuscript.

Competing interests

The authors declare no competing interests.

Additional information

Supplementary information is available for this paper at https://doi.org/10.1038/s41557-020-0493-5.

Correspondence and requests for materials should be addressed to S.J.W., A.C. or B.L.F.